



TFBGs in polyimide-coated optical fibers for multi-parameter measurements

HANG QU,¹ SHAOXIN MA,¹ CARLOS MARQUES,^{2,3}  CHRISTOPHE CAUCHETEUR,⁴  AND XUEHAO HU^{4,*} 

¹Research Center for Advanced Optics and Photoelectronics, Department of Physics, College of Science, Shantou University, Shantou 515063, China

²CICECO – Aveiro Institute of Materials, Physics Department, University of Aveiro, 3810-193 Aveiro, Portugal

³Department of Physics, VSB – Technical University of Ostrava, Ostrava 70800, Czech Republic

⁴Department of Electromagnetism and Telecommunication, University of Mons, Boulevard Dolez 31, 7000 Mons, Belgium

*xuehao.hu@umons.ac.be

Abstract: Tilted fiber Bragg gratings (TFBGs) contain core and cladding modes and can be used to measure several environmental parameters. However, most of the research to date has focused on stripped single-mode fiber while the preservation of the coating can be highly relevant in practice, especially in harsh environments. In this paper, we use a femtosecond laser direct writing technique to inscribe a 12-degree tilted grating directly into a polyimide (PI)-coated single-mode fiber, where the PI coating keeps the fiber intact and robust. The protective coating layer also acts as a Fabry-Perot cavity and induces a periodic amplitude modulation of the cladding mode resonances. The latter behaves differently compared to mode resonances in response to different measurands. In this work, measurements of temperature, strain and surrounding refractive index are presented.

© 2025 Optica Publishing Group under the terms of the [Optica Open Access Publishing Agreement](#)

1. Introduction

In recent years, fiber-optic sensor technology has been extensively studied and used for measuring various physical and chemical parameters, including temperature [1,2], strain [3], displacement [4,5], humidity [6], refractive index [7], gases [8] and salinity [9]. Fiber-optic sensors offer numerous advantages, encompassing immunity to electromagnetic interference, lightweight construction, compact structure, high sensitivity, wide bandwidth, and the simplicity of signal transmission through optical means. Of the diverse fiber-optic sensor architectures, fiber Bragg grating (FBG) sensors stand out as one of the most prevalent technologies, with their operation relying on axially periodic refractive index modulations photo-inscribed within the fiber core.

Traditionally, FBGs are fabricated by ultraviolet (UV) laser phase mask technique, but this method generally requires pre-treatment of the optical fibers with hydrogen-loading process to increase the photosensitivity of the fiber core or the use of highly photosensitive optical fibers. The inscribed gratings produced through this method are normally thermally unstable, and the grating period is limited by the pitch of the mask plate [10,11]. However, femtosecond (fs) laser direct writing enables the fabrication of FBGs within any type of optical fiber without fiber pre-treatment. Laser direct writing techniques comprise three methods: line-by-line (LbL), point-by-point (PbP), and plane-by-plane (Pl-b-Pl). Unlike the phase-mask technique, fs-laser direct writing provides significant design flexibility in choosing Bragg wavelengths and grating lengths [12]. Moreover, these gratings can survive high temperatures and sensing up to 1000 °C has been previously reported [13]. FBG and its derivative sensors have been employed to measure a wide range of physical parameters, including vibration, displacement, acceleration, pressure,

strain, temperature and tilt. Their relevant application fields include structural monitoring, mechanical engineering, electrical engineering, aerospace engineering, among others [14,15].

Compared to traditional FBGs, tilted FBGs (TFBGs) [16] bring the unique capability to detect bending and surrounding refractive index (SRI) changes due to their ability to excite cladding mode resonances resulting from the coupling between core and cladding modes. For SRI measurements, TFBGs can inherently provide temperature compensation, as the core mode confined within the optical fiber core demonstrates immunity to SRI changes [16].

Typically, TFBGs are manufactured using phase mask technique or fs-laser direct writing technique, similar to the fabrication of standard FBGs [16]. Recently, fs laser LbL method has been used for TFBG in both silica optical fibers [17] and polymer optical fibers [18]. The cladding modes of the TFBGs are highly sensitive to external influences, exhibiting remarkably heightened detection sensitivity and resolution, facilitating precise detection across various physical, mechanical, electromagnetic, biological, medical, and chemical parameters, like through innovative structural designs, physical combinations, and biochemically modified materials [16,19,20].

Recently, advancements of TFBG applications have been reported, especially in lithium-ion battery monitoring and refractive index demodulation. For instance, Liu *et al.* demonstrated TFBG sensors to track, via the monitoring of both temperature and refractive index metrics, electrolyte-electrode coupled changes involved in the charge-discharge process of lithium sulfur batteries [21]. Han *et al.* introduced an ultrasensitive TFBG sensor for *in situ* monitoring of lithium dendrite growth and mass transport kinetics at the interface of lithium anodes to understand and link the nanoscale ion and solid-electrolyte-interphase (SEI) behavior with the macroscopic battery performances [22]. In terms of surface refractive index demodulation, Fasseaux *et al.* introduced a machine learning-based regression model with gold-coated TFBG sensors. This approach offers a universal route for calibration of TFBG-based surface plasmon resonance (SPR) sensors, enabling a correlation between spectral shifts and refractive index changes [23]. In all these applications, gratings manufactured by standard writing techniques were used, implying that the coating layer of the fiber is removed within the grating inscription area. Relying on through-coating inscribed TFBGs could be much preferable in practice, especially to preserve the pristine fiber robustness during sensing applications. Abdukerim *et al.* inscribed TFBG through the polyimide (PI) coating using a fs laser and phase mask technique. However, the amplitude of cladding modes was limited to below ~5 dB. The work mainly focused on investigation of inscription method [24].

In this paper, we utilized the fs-laser direct writing technique to inscribe 12-degree TFBGs in a single-mode fiber through a PI coating layer. The preservation of the intact coating layer maintains the mechanical strength of the fiber. Additionally, due to the coupling of the core and cladding modes, along with the PI coating acting as a Fabry-Perot (F-P) cavity, TFBGs exhibit an interesting periodic amplitude modulation phenomenon of the cladding mode resonance. A series of samples were prepared and characterized for temperature, axial strain and surrounding refractive index (SRI) sensing. To determine the temperature sensitivity, the gratings were immersed in a water bath and their temperature was changed between 20.2 °C and 41.5 °C. The recorded temperature sensitivities were 13.7 ± 0.1 pm/°C, 13.2 ± 0.2 pm/°C, 8.9 ± 0.1 pm/°C, and -25 ± 1 pm/°C for the core, ghost, cladding modes, and the envelope, respectively. The strain sensitivity was examined in the range 0 to 10000 $\mu\epsilon$. The sensitivities of the core and ghost modes were 0.794 ± 0.006 pm/ $\mu\epsilon$ and 0.808 ± 0.004 pm/ $\mu\epsilon$, respectively. The sensitivities of the cladding mode and the envelope were 0.673 ± 0.003 pm/ $\mu\epsilon$ and 0.605 ± 0.006 pm/ $\mu\epsilon$, respectively. The SRI characterization of the TFBG was carried out in a large range between 1.30~1.54. For measurements of SRI, the amplitude of the envelope exponentially decreases with increasing SRI, and the sensitivity characterized at the cutoff wavelength was 500 ± 100 nm/RIU in the range of 1.30~1.34. For a smaller SRI range of 1.3331~1.3925, the intensity of one cladding mode at 1522.1 nm increased with the increase of SRI, exhibiting a sensitivity of 17 ± 1 dB/RIU,

and the wavelength of another cladding mode at 1564.2 nm red-shifted with the increase of SRI, with a sensitivity of 3.1 ± 0.2 nm/RIU.

2. Principle

2.1. Operation principle of TFBG

TFBGs are categorized as short period (~ 500 nm) gratings with a refractive index modulation direction slightly angled with respect to the optical fiber axis. TFBGs have two mode-coupling mechanisms: self-backward coupling of the core mode and backward couplings between the core mode and numerous cladding modes [25]. The former generates Bragg mode or core mode similarly as regular FBGs, and the Bragg wavelength λ_{Bragg} is expressed as:

$$\lambda_{Bragg} = 2n_{eff,core}\Lambda \quad (1)$$

where $n_{eff,core}$ denotes the effective refractive index of the core mode, and Λ represents the grating period along the fiber axis.

For the backward coupling, TFBGs enable light to propagate in the cladding with varying angles corresponding to different effective refractive indices of cladding modes, $n_{eff,clad}^i$. Thus, wavelength of the cladding mode resonance is in one-to-one correspondence with its effective refractive index. This relationship could be expressed by the following phase-matching condition:

$$\lambda_{clad}^i = (n_{eff,core} + n_{eff,clad}^i)\Lambda \quad (2)$$

where the superscript i denotes the cladding mode number.

The ghost mode, which is the cladding mode nearest to the core mode, is formed by the combination of several low-order cladding modes [16].

2.2. Principle of F-P interferometer for cladding mode modulation in PI-coated TFBG

In PI-coated TFBGs, there are two parallel interfaces, which are the cladding-coating interface S_1 and the coating-surrounding medium interface S_2 . While the core mode remains confined within the core of the TFBG, part of the cladding modes may penetrate into the coating layer, thus exciting the resonant F-P modes thereby. Using ray optics, we could consider a cladding mode as a ray incident to S_1 with an angle of θ_1 (see Fig. 1). Thus, the ray would then refract with an angle of θ_2 according to Snell's Law. The resonant condition for constructive interference could be expressed as [26]

$$2nd \cdot \cos\theta_2 = m\lambda_m \quad (3)$$

where d is the thickness of the PI coating layer, n is the refractive index of PI, λ_m is the wavelength of m_{th} order F-P interference. Hence, the intensity of the cladding modes is periodically modulated. The free spectral range (FSR) of the F-P interferometer is an important spectral characteristic, which characterizes the wavelength interval between adjacent interference peaks/valleys in the spectrum and can be calculated by the following formula:

$$FSR = \frac{\lambda_m^2}{2nd \cdot \cos\theta_2} \quad (4)$$

The illustration of the principle including TFBG and F-P interferometer are shown in Fig. 1.

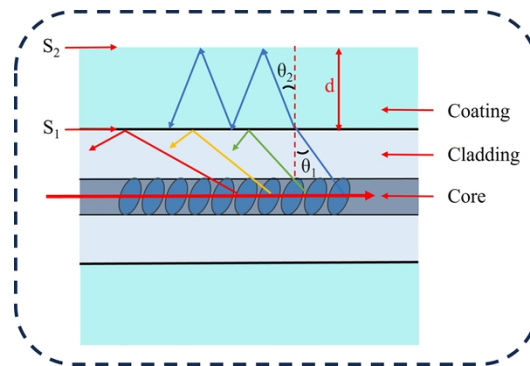


Fig. 1. Illustration of the principle including TFBG and F-P interferometer.

3. Experimental results

3.1. Sensor probe fabrication

The fiber used in this work is SM1500 (7.8/125)P supplied by Fibercore Inc. The actual diameters of the mode field, the fiber and the PI coating are $7.7\ \mu\text{m}$, $125\ \mu\text{m}$ and $158\ \mu\text{m}$, respectively. As the TFBGs were inscribed through the PI coating of the fiber, the integrity and robustness of the fiber remained, which is beneficial for the usage of the sensor probe.

The TFBG inscription system is sketched in Fig. 2. The fs laser (SpOne-8-SHG, Newport) emits pulses at $520\ \text{nm}$ with a pulse duration of $346\ \text{fs}$ and a maximal repetition rate of $200\ \text{kHz}$. The fiber sample was immobilized on a multi-axis tilt platform (M-37, Newport) integrated on a three-axis precision translation stage (X/Y: XMS100-S, Z: M-VP-5ZA, Newport). An oil-immersion objective ($60\times$, $\text{NA} = 1.42$, UPLXAPO60XO, Olympus) was used to focus the laser beam onto the central core of the fiber. The oil used in this work is a refractive index matching solution from Olympus a refractive index of 1.515 .

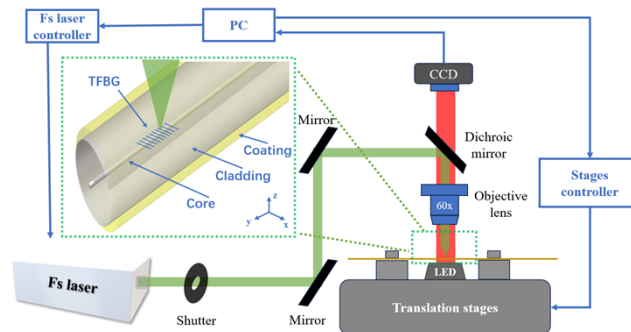
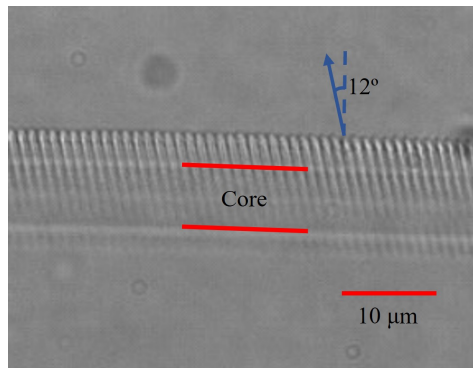
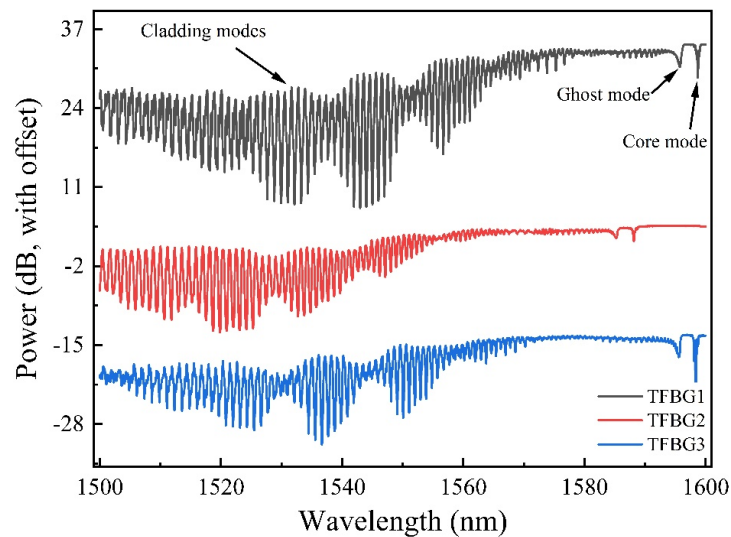


Fig. 2. Illustration of the setup for LbL TFBG inscription.

Gratings were fabricated by fs-laser LbL inscription technique. Each grating line has a length of $12\ \mu\text{m}$ across the central core with a tilt angle of 12° . The laser pulse energy, repetition rate, and scanning speed were set at $\sim 33\ \text{nJ}$, $500\ \text{Hz}$, and $100\ \mu\text{m/s}$, respectively. Three TFBGs were inscribed and employed for measurements of temperature, strain, and refractive index, respectively, as shown in Table 1. A microscope image of TFBG 1 is presented in Fig. 3, clearly showing refractive index modifications induced by the fs-laser. The transmitted spectra were monitored by an FBG interrogator (FS22SI, HBM Fiber Sensing) featuring a wavelength resolution of $1\ \text{pm}$ and a scanning rate of $1\ \text{Hz}$. The spectra of TFBGs 1-3 are shown in Fig. 4,

Table 1. TFBG inscription parameters using fs LbL technique

	Measurement	Grating period (μm)	Number of Period	Grating length (mm)
TFBG 1	Temperature	1.103	7000	7.7
TFBG 2	Strain	1.096	5000	5.5
TFBG 3	Refractive index	1.103	5000	5.5

**Fig. 3.** Microscopic image of TFBG 1 inscribed by the fs-laser at 520 nm. The two red lines in the center of this image represent the core-cladding interfaces.**Fig. 4.** The transmitted spectra of TFBGs 1-3 (vertical offset for visual separation) with a core mode, a ghost mode, and a periodic amplitude modulation of cladding mode resonances.

clearly exhibiting a core mode, a ghost mode, and cladding mode resonances with a periodic amplitude modulation, i.e., envelope of cladding modes. The latter results from the coupling of cladding modes into the PI layer, which serves as a F-P resonator. It is worth mentioning that according to phase-matching condition Eq. (2), cladding modes centered at ~ 1550 nm (shorter in wavelength than the core mode) exhibit smaller effective refractive indices, enabling the calculation of the incident angle θ_1 of the ray at S_1 interface. Then, according to Snell's Law, the refraction angle θ_2 of cladding modes is smaller than θ_1 , as the refractive index of the silica cladding ~ 1.44 [27] is smaller than PI coating ~ 1.50 [28]. In the following paragraphs, the core mode, the ghost mode, the single cladding mode and the envelope of the cladding modes will be characterized in temperature, strain and refractive index measurements.

3.2. Temperature measurement

TFBG 1 was immersed in a water-filled 3D printed reservoir, which was placed on a temperature-controlled breadboard (PTC1/M, Thorlabs). The temperature of the breadboard was adjusted from 20°C to 45°C with a step of 5°C . The TFBG temperature was also monitored by measuring the water temperature using a thermocouple probe. Note that the PI coating can absorb water [29] which somehow would disturb temperature measurement. The grating was kept in water for around 2 hours at the initial temperature of 20°C to ensure that the water content absorbed by the coating was saturated, which was proved by the stable spectra of the sensor. Afterwards, the temperature of the grating was increased as proposed above. At each temperature, the grating was immersed in water for ~ 20 minutes to have its transmitted spectrum fully stabilized.

Figure 5 records the wavelength shift of the fiber core mode (at ~ 1598.77 nm) and a single cladding mode (at ~ 1542.17 nm) during the whole temperature characterization process, and the transmitted spectrum is recorded every 30 s. It can be seen that the patterns of wavelength shift of the fiber core mode and the cladding mode are quite similar and synchronized. The wavelengths are red-shifted with increased temperatures. The sudden wavelength changes between two adjacent temperatures result from the sudden temperature changes of the breadboard and(or) the added water maintaining the grating underwater. The evolution of the enveloped transmitted

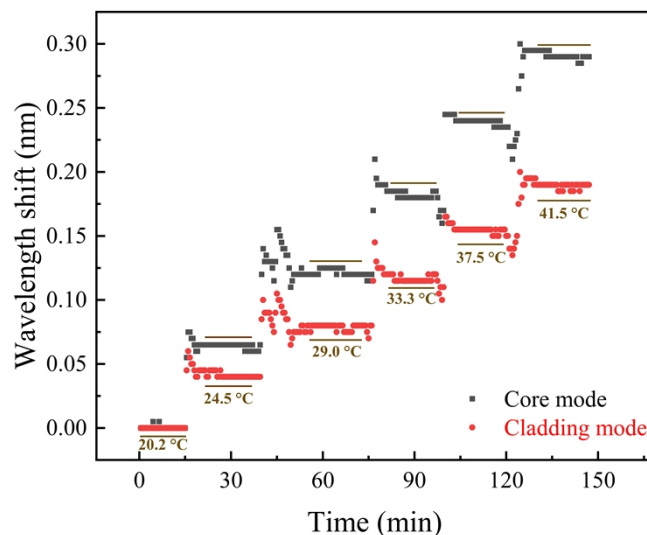


Fig. 5. The wavelength evolution of the core mode at ~ 1598.77 nm and the cladding mode at ~ 1542.17 nm in the temperature range of 20.2 to 41.5°C . Each individual spectrum was recorded every 30s intervals.

spectra as a function of temperature is illustrated in Fig. 6. The envelope exhibits a blue-shift trend from 20.2 °C to 41.5 °C.

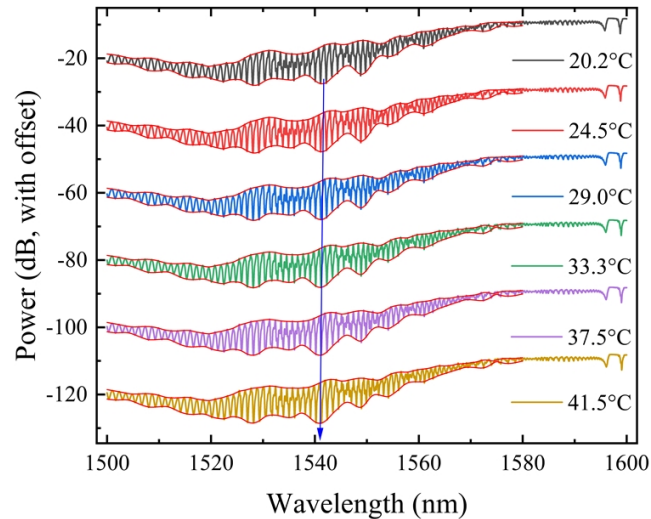


Fig. 6. Transmitted spectral (with envelope) evolution of TFBG 1 during the temperature experiment from 20.2 °C to 41.5 °C (vertical offset for visual separation).

The red-shifts of spectra of the core mode, ghost mode and cladding mode in response to increasing temperatures are shown in Fig. 7(a)-(c), which can be explained by the positive thermo-optic coefficient (TOC) ($\sim 9.2 \times 10^{-6}/^{\circ}\text{C}$) of the quartz silica [30] of the fiber core and the cladding. On the other hand, the spectral envelope had a blue shift, which could be explained

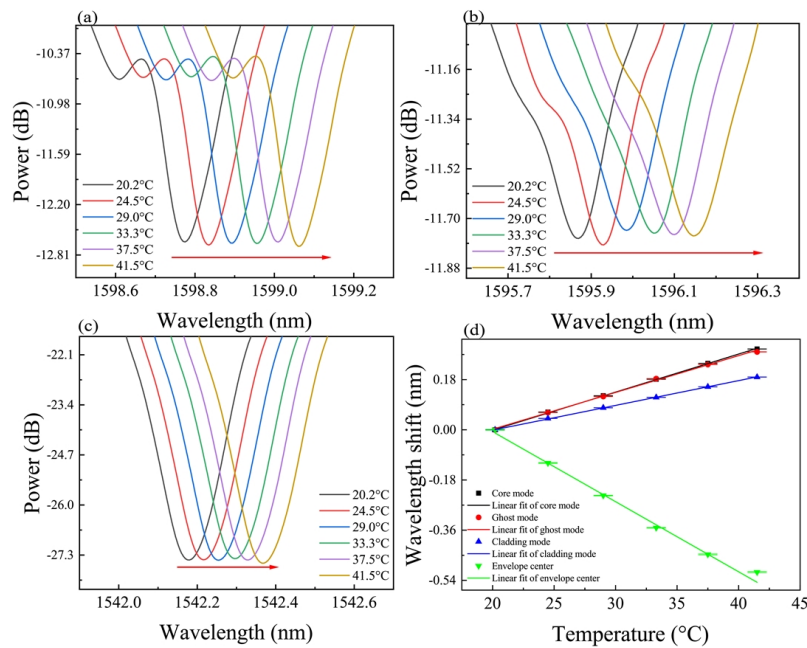


Fig. 7. (a) Spectral evolution of the core mode at ~ 1598.7 nm. (b) Spectral evolution of the ghost mode at ~ 1595.8 nm. (c) Spectral evolution of the individual cladding mode at ~ 1542.1 nm. (d) Linear regression analysis on the experimental results for the temperature ranging from 20.2 to 41.5 °C.

by the negative TOC ($-4.6 \times 10^{-5}/^{\circ}\text{C}$) of the polymer coating layer [31]. According to Eq. (3), when the refractive index n of this coating layer decreases with elevating temperature, and the center wavelength λ_m of the interference dip shifts toward shorter wavelengths.

Figure 7(d) shows the linear fitting of resonant wavelength of the core mode, ghost mode, cladding mode and spectral envelope in response to temperature variations. An error bar analysis was performed on these data, and the spectra within 15 minutes of each temperature stabilization were selected for analysis. It is worth noting that the errors in sensitivity, wavelength, and power mentioned throughout this paper refer to the standard error. The sensitivity of the core mode is $13.7 \pm 0.1 \text{ pm}/^{\circ}\text{C}$, while the counterpart of the ghost mode (with similar properties of the core mode [16]) is $13.2 \pm 0.2 \text{ pm}/^{\circ}\text{C}$. However, the sensitivity of the cladding mode is $8.9 \pm 0.1 \text{ pm}/^{\circ}\text{C}$, which is smaller than the core mode and the ghost mode. This phenomenon could be explained by the different material properties of the cladding and coating layers, which have TOCs of opposite signs. As the temperature rises, the red shift of the cladding mode is alleviated. The envelope has a high temperature sensitivity of $-25 \pm 1 \text{ pm}/^{\circ}\text{C}$.

3.3. Strain measurement

To perform strain characterization, both ends of TFBG 2 were fixed onto two translation stages (TSDH-601C, SIGMAKOKI, JAPAN). Particularly, one end was kept still, and the other end was displaced with different fiber strains. The evolution of the transmitted spectra was recorded from 0 to 10000 $\mu\epsilon$ with a step of $\sim 1000 \mu\epsilon$. The wavelength variations of the core mode and the cladding mode during the whole process of strain characterization are shown in Fig. 8, including the stretching motions and the strain-holding process. Each spectrum was recorded every 2 s. It can be seen that the wavelength shifts of the core mode and the cladding mode are generally similar and synchronized. In general, their wavelengths red-shifted with increasing strains. However, during each individual stretching process, the wavelength firstly red-shifted, and then slowly blue-shifted until gradual stabilization, the whole process lasted about 15 minutes. This phenomenon could be explained by the fact that during each stretching process, the bare silica fiber first moved simultaneously with the coating and then the bare fiber gradually shrunk due to the creep deformation of the polymer layer.

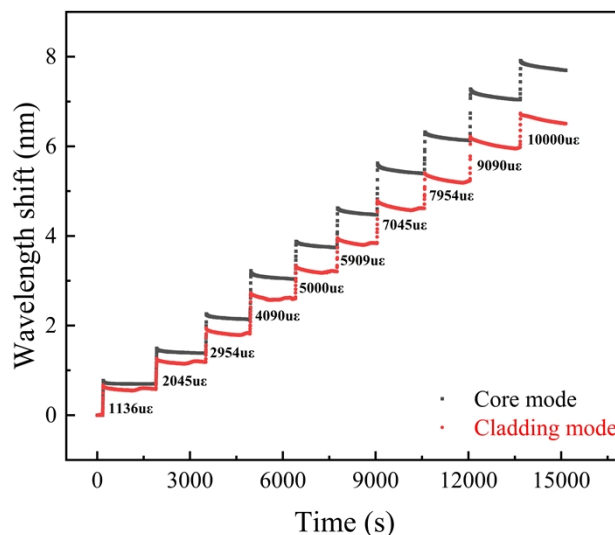


Fig. 8. The spectral wavelength evolution of the core mode at $\sim 1588.025 \text{ nm}$ and the cladding mode at $\sim 1530.2 \text{ nm}$ in the strain range of 0 to 10000 $\mu\epsilon$. Each individual spectrum was recorded every 2 s intervals.

The spectral evolutions were shown in Fig. 9. It can be seen that the envelope of the spectra red-shifted as a function of strain, which can be mainly attributed to the increase of $nd \cdot \cos\theta_2$ with increasing strain according to Eq. (3). The refractive index n of the coating is related to the applied strain due to the elasto-optic effect [32,33], the thickness of the coating d decreases with strain, and the angle of refraction θ_2 is decided by both indices of the coating and the silica cladding, which are influenced by the strain.

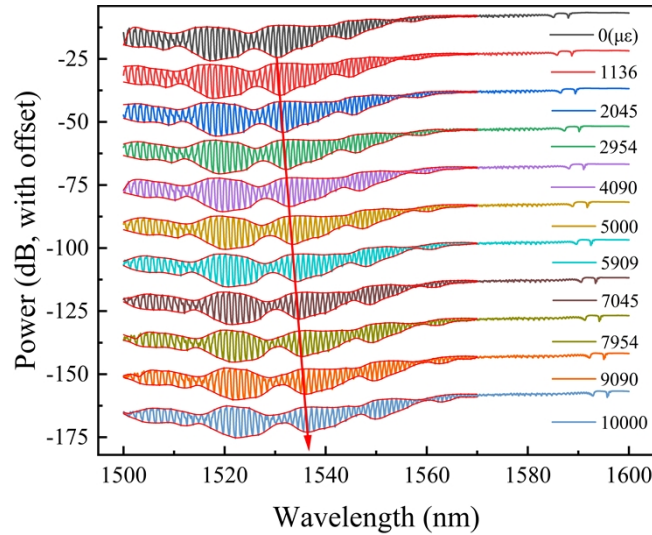


Fig. 9. Experimental spectral evolution of TFBG 2 for the strain ranging from 0 to 10000 $\mu\epsilon$ (vertical offset for visual separation).

The red-shifts of spectra of the core mode, ghost mode and cladding mode are shown Fig. 10(a)-(c). Figure 10(d) shows the strain sensitivities of the core, ghost, cladding mode and envelope after linear fitting. This fitting procedure was done with an error bar analysis to record the spectra for 5 minutes after stabilization of each strain process. It can be seen that the sensitivity of the envelope and cladding mode are similar, which are 0.605 ± 0.006 pm/ $\mu\epsilon$ and 0.673 ± 0.003 pm/ $\mu\epsilon$, respectively. The sensitivity of the core mode is 0.794 ± 0.006 pm/ $\mu\epsilon$, and the corresponding value for the ghost mode with similar properties of the core mode is 0.808 ± 0.004 pm/ $\mu\epsilon$.

3.4. Refractive index measurement

The refractive index measurement was conducted by immersing the sensing probe (TFBG 3) successively in a series of calibrated liquids (Cargille oils) with different (refractive indices) RIs covering a large range from 1.30 to 1.54, with an interval of 0.02. Transmitted spectra are presented in Fig. 11.

It can be clearly seen that the cladding modes at short wavelength disappear when the probe was immersed in the solutions with RIs from 1.30 to 1.34. By monitoring the cut-off wavelength of cladding modes, a refractometric sensitivity of 500 ± 100 nm/RIU was obtained, as shown in Fig. 12(a). However, with higher RIs, the cladding modes were all maintained with an almost constant cut-off wavelength, and the amplitude of the cladding mode decreases. The maintained cut-off wavelength of cladding mode could be attributed to the PI cavity, which enables the light reflected between S_1 and S_2 interfaces. Thus, only part of light is refracted into the surrounding medium. The decrease of the cladding mode amplitude could be due to the decrease of the RI difference at the coating-surrounding medium interface S_2 . The latter reduced the amplitude of

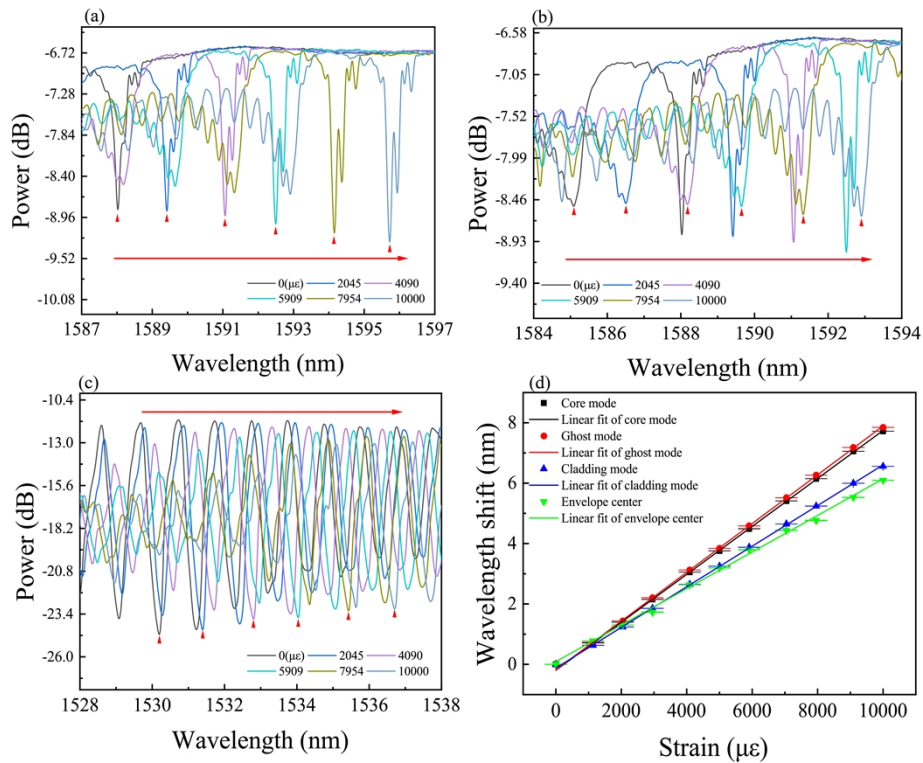


Fig. 10. Evolutions of the core mode at ~1588.0 nm (a), the ghost mode at ~1585.1 nm (b) and the cladding mode at ~1530.2 nm (c), linear regression analysis on the experimental results for the strain ranging from 0 to 10000 $\mu\epsilon$ (d).

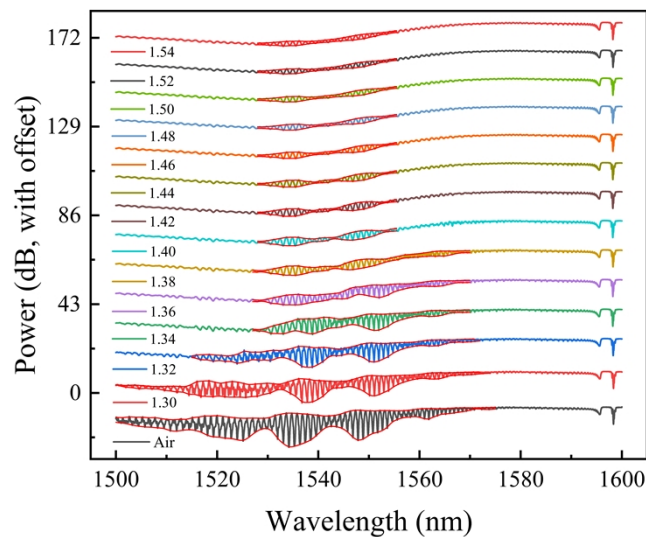


Fig. 11. Experimental spectrum evolution of TFBG 3 at refractive index ranging from 1 to 1.54 RIU (vertical offset for visual separation).

the propagating cladding mode, mitigating the core-cladding mode couplings. An exponential fitting of the cladding mode amplitude with SRI is shown in Fig. 12(b).

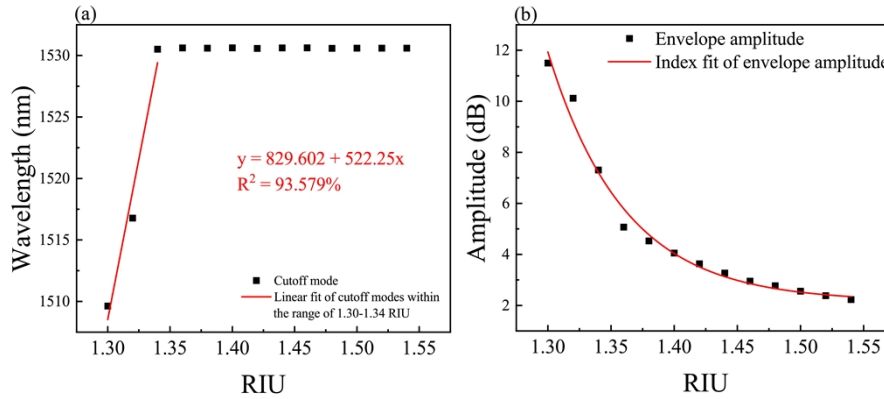


Fig. 12. (a) Evolution of cutoff mode wavelength with SRI from 1.30 to 1.54. (b) Exponential fit analysis of envelope amplitudes in the 1.30 to 1.54 SRI range.

Next, experiments were performed in a glucose-water solution. The TFBG 3 was immersed in water in the 3D-printed reservoir, and since the PI coating absorbs water and interferes with the refractive index measurements, the grating was first kept in the water for about 2 hours to ensure that water absorption of the polymer coating got saturated and transmission spectrum no longer shifted. Also note that during the whole SRI characterization, the grating was always immersed in the glucose solution, even when SRI was changed. Additionally, SRI of the solutions was monitored in real time by an Abbe refractometer (PAL-RI, ATAGO) to ensure that it reached a steady state, and the spectra were recorded for half an hour after each SRI was stabilized. The evolution of the transmission spectra for solutions with RIs ranging from 1.3331 to 1.3925 RIU is shown in Fig. 13(a).

Figure 13(b),(c) demonstrates the variations in the wavelength of the fiber core mode and the ghost mode with increasing SRI, and it can be seen that both are insensitive to the refractive index. Figure 13(d),(e) demonstrates the variation of the intensity of the cladding mode at 1522.1 nm and the wavelength of the cladding mode at 1564.2 nm with increasing SRI, and it can be seen that the wavelength of the cladding mode at 1522.1 nm drifted less while the intensity became larger with increasing SRI. On the other hand, the cladding mode at 1564.2 nm behaves in the opposite way. With increasing SRI, its intensity changed less while the wavelength underwent a significant red shift. Figure 13(f) shows the refractive index sensitivity of the two cladding modes after linear fitting. An error bar analysis was performed on these data, with spectra selected for analysis within 30 minutes of stabilization at each SRI. The cladding mode at 1522.1 nm demonstrates an intensity sensitivity of 17 ± 1 dB/RIU, whereas the cladding mode at 1564.2 nm exhibits a wavelength sensitivity of 3.1 ± 0.2 nm/RIU.

4. Discussion

Table 2 displays the comparison of temperature, strain and refractive index sensitivities between coated and uncoated TFBGs. Although generally the sensitivities of this work are not outstanding, the temperature sensitivity of the cladding envelope is relatively high. In addition, the significant difference in sensitivity among different modes may be more conducive to the simultaneous measurement of multiple parameters [38]. Moreover, we retained the coating and enhanced the mechanical strength.

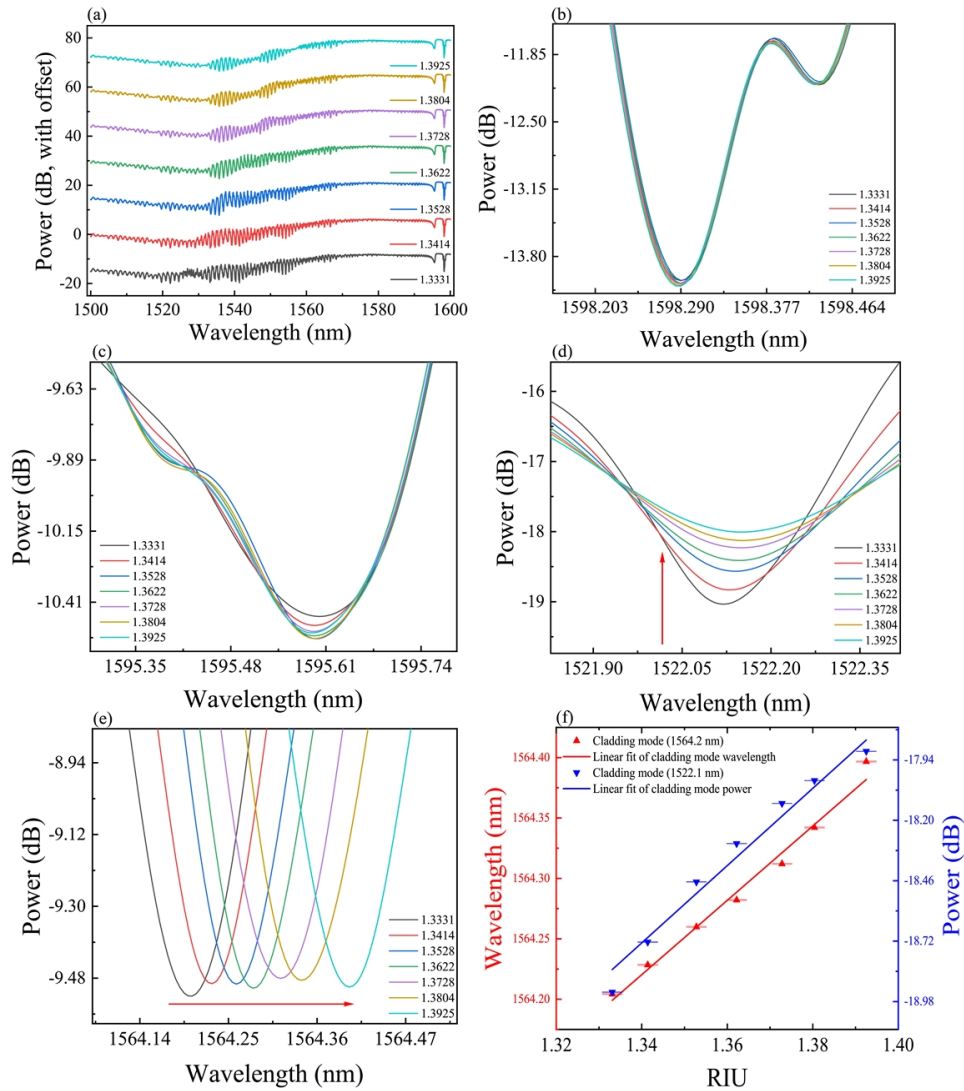


Fig. 13. (a) Experimental spectrum evolution of TFBG3 at refractive index ranging from 1.3331 to 1.3925 RIU (vertical offset for visual separation). (b) Spectral evolution of the core mode at ~1598.2 nm. (c) Spectral evolution of the ghost mode at ~1595.6 nm. (d) Spectral evolution of the cladding mode at ~1522.1 nm. (e) Spectral evolution of the cladding mode at ~1564.2 nm. (f) Linear regression analysis on the experimental results for the SRI ranging from 1.3331 to 1.3925 RIU.

Table 2. Comparison of temperature, strain and refractive index sensitivities between coated and uncoated TFBGs

	Measurement range	Core mode	Ghost mode	Cladding mode	Cladding envelope	Ref.
Uncoated TFBG	20~70 °C 0~1464 $\mu\epsilon$	8.5 pm/°C 1.03 pm/ $\mu\epsilon$	9.8 pm/°C 1.03 pm/ $\mu\epsilon$			[34]
Uncoated TFBG	1.30~1.45 RIU			500 nm/RIU		[35]
Uncoated TFBG	25~175 °C 0~4500 $\mu\epsilon$	4.2 pm/°C 0.816 pm/ $\mu\epsilon$		6.02 pm/°C 0.83 pm/ $\mu\epsilon$		[36]
Uncoated TFBG	1.30~1.45 RIU			510.48 nm/RIU		[37]
PI-coated TFBG	20~60 °C 0~1100 $\mu\epsilon$	10.7 pm/°C 0.947 pm/ $\mu\epsilon$		10.2 pm/°C 1.35 pm/ $\mu\epsilon$		[3]
PI-coated TFBG	20~45 °C 0~10000 $\mu\epsilon$ 1.30~1.34 RIU	13.7 pm/°C 0.794 pm/ $\mu\epsilon$	13.2 pm/°C 0.808 pm/ $\mu\epsilon$	8.9 pm/°C 0.673 pm/ $\mu\epsilon$ 500 nm/RIU	-25 pm/°C 0.605 pm/ $\mu\epsilon$	This work

5. Conclusion

In summary, a structurally simple and robust PI-coated TFBG fiber sensor is presented, which enables simultaneous measurement of temperature, strain and refractive index. The TFBG was inscribed in the single-mode fiber with a PI coating layer, which makes the fiber mechanically strong and can be better used in various complex environments. Moreover, based on TFBG to excite cladding modes and the coupling of the cladding modes into the F-P cavity formed by the PI coating, the sensor probe exhibited cladding mode resonance with periodic amplitude modulation envelopes. Three TFBG-probes were characterized for temperature, strain, and refractive index measurements. The sensitivities of the core and ghost modes, the cladding modes and the envelopes were investigated. Their distinct sensing properties paved the way for simultaneous multiparameter sensing applications. Finally, as the PI coating could be converted via laser irradiation into graphene with relatively high surface area and conductivity [39,40], PI-coated fibers with TFBGs may exhibit promising potentials for electrochemical/biomedical sensing applications.

Funding. National Natural Science Foundation of China (62475140); Guangxi Key Laboratory of Optoelectronic Information Processing (GD23203); Fonds de la Recherche Scientifique (F.R.S.-FNRS) (Postdoctoral Researcher grant, Chargé de Recherches); European Union, REFRESH – Research Excellence For REgion Sustainability and High-tech Industries (CZ.10.03.01/00/22_003/0000048, Operational Programme Just Transition); Portuguese Science and Technology Foundation/MCTES (FCT I.P.) (CICECO, LA/P/0006/2020, UIDB/50011/2020, UIDP/50011/2020).

Acknowledgments. We acknowledge funding from the National Natural Science Foundation of China (62475140); Guangxi Key laboratory of Optoelectronic Information Processing (GD23203); The Fonds de la Recherche Scientifique (F.R.S.-FNRS) under the Postdoctoral Researcher grant (Chargé de Recherches) of Xuehao Hu and the Research Director Position of Christophe Caucheteur. The research was co-funded by the financial support of the European Union under the REFRESH – Research Excellence For REgion Sustainability and High-tech Industries project number CZ.10.03.01/00/22_003/0000048 via the Operational Programme Just Transition. This work was also developed within the scope of the projects CICECO (LA/P/0006/2020, UIDB/50011/2020 & UIDP/50011/2020) financed by national funds through the (Portuguese Science and Technology Foundation/MCTES (FCT I.P.)).

Disclosures. The authors declare no conflicts of interest.

Data availability. Data underlying the results presented in this paper are not publicly available at this time but may be obtained from the authors upon reasonable request.

References

1. X. Wang, X. Sun, Y. Hu, *et al.*, “Highly-sensitive fiber Bragg grating temperature sensors with metallic coatings,” *Optik* **262**, 169337 (2022).
2. H. Huang, X. Zhu, C. Jiang, *et al.*, “High sensitivity temperature sensor based on enhanced Vernier effect through two parallel Fabry-Perot cavities,” *Appl. Opt.* **62**(2), 275–283 (2023).
3. S. Takeda, M. Sato, and T. Ogasawara, “Simultaneous measurement of strain and temperature using a tilted fiber Bragg grating,” *Sens. Actuators, A* **335**, 113346 (2022).
4. M. Lomer, J. Zubia, J. Arrue, *et al.*, “Principle of functioning of a self-compensated fibre-optical displacement sensor based on diffraction-grating-ended POF,” *Meas. Sci. Technol.* **15**(8), 1474–1478 (2004).
5. X. Wen, T. Ning, Y. Bai, *et al.*, “High-Sensitive Microdisplacement Sensor Based on Fiber Mach-Zehnder Interferometer,” *IEEE Photonics Technol. Lett.* **26**(23), 2395–2398 (2014).
6. T. L. Yeo, T. Sun, and K. T. V. Grattan, “Fibre-optic sensor technologies for humidity and moisture measurement,” *Sens. Actuators, A* **144**(2), 280–295 (2008).
7. T. Hu, Y. Zhao, and A.-n. Song, “Fiber optic SPR sensor for refractive index and temperature measurement based on MMF-FBG-MMF structure,” *Sens. Actuators, B* **237**, 521–525 (2016).
8. G. Yan, A. P. Zhang, G. Ma, *et al.*, “Fiber-Optic Acetylene Gas Sensor Based on Microstructured Optical Fiber Bragg Gratings,” *IEEE Photonics Technol. Lett.* **23**(21), 1588–1590 (2011).
9. G. Li, Y. Wang, A. Shi, *et al.*, “Review of Seawater Fiber Optic Salinity Sensors Based on the Refractive Index Detection Principle,” *Sensors* **23**(4), 2187 (2023).
10. Y. Masuda, M. Nakamura, C. Komatsu, *et al.*, “Wavelength evolution of fiber Bragg gratings fabricated from hydrogen-loaded optical fiber during annealing,” *J. Lightwave Technol.* **22**(3), 934–941 (2004).
11. C. L. Liou, L. A. Wang, and M. C. Shih, “Characteristics of hydrogenated fiber Bragg gratings,” *Appl. Phys. A* **64**(2), 191–197 (1997).
12. L. Liu, X. Li, Y. Xu, *et al.*, “Direct femtosecond laser writing fiber Bragg gratings in double-D cladding chalcogenide glass infrared fibers,” *Opt. Laser Technol.* **174**, 110586 (2024).
13. P. Jiang, Q. Xu, R. Zhang, *et al.*, “High-temperature and stress response behavior of femtosecond laser pulses inscribed eccentric fiber Bragg gratings,” *Heliyon* **9**(6), e17185 (2023).
14. J. Sahota, N. Gupta, and D. Dhawan, “Fiber Bragg grating sensors for monitoring of physical parameters: a comprehensive review,” *Opt. Eng.* **59**(06), 1 (2020).
15. A. Shadab, S. K. Raghuvanshi, and S. Kumar, “Advances in Micro-Fabricated Fiber Bragg Grating for Detection of Physical, Chemical, and Biological Parameters—A Review,” *IEEE Sens. J.* **22**(16), 15650–15660 (2022).
16. J. Albert, L.-Y. Shao, and C. Caucheteur, “Tilted fiber Bragg grating sensors,” *Laser Photonics Rev.* **7**(1), 83–108 (2013).
17. H. Li, X. Zhao, B. Rao, *et al.*, “Fabrication and Characterization of Line-by-Line Inscribed Tilted Fiber Bragg Gratings Using Femtosecond Laser,” *Sensors* **21**(18), 6237 (2021).
18. H. Qu, Z. Chen, S. Gao, *et al.*, “Femtosecond laser line-by-line tilted Bragg grating inscription in single-mode step-index TOPAS/ZEONEX polymer optical fiber,” *Opt. Lett.* **48**(6), 1438–1441 (2023).
19. H. Jean-Ruel and J. Albert, “Recent advances and current trends in optical fiber biosensors based on tilted fiber Bragg gratings,” *Trends Anal. Chem.* **174**, 117663 (2024).
20. O. V. Butov, K. A. Tomyshev, I. A. Nechepurenko, *et al.*, “Tilted fiber Bragg gratings and their sensing applications,” *Phys. Usp.* **65**(12), 1290–1302 (2022).
21. F. Liu, W. Lu, J. Huang, *et al.*, “Detangling electrolyte chemical dynamics in lithium sulfur batteries by operando monitoring with optical resonance combs,” *Nat. Commun.* **14**(1), 7350 (2023).
22. X. Han, H. Zhong, K. Li, *et al.*, “Operando monitoring of dendrite formation in lithium metal batteries via ultrasensitive tilted fiber Bragg grating sensors,” *Light: Sci. Appl.* **13**(1), 24 (2024).
23. H. Fasseaux, M. Loyez, and C. Caucheteur, “Machine learning unveils surface refractive index dynamics in comb-like plasmonic optical fiber biosensors,” *Commun. Eng.* **3**(1), 34 (2024).
24. N. Abdukerim, D. Grobncic, C. Hnatovsky, *et al.*, “Through-the-coating writing of tilted fiber Bragg gratings with the phase mask technique,” *Opt. Express* **27**(26), 38259–38269 (2019).
25. T. Erdogan, “Fiber grating spectra,” *J. Lightwave Technol.* **15**(8), 1277–1294 (1997).
26. T.-A. Chen, M.-J. Yub, Y.-J. Lu, *et al.*, “Ultra-broadband, lithography-free, omnidirectional, and polarization-insensitive perfect absorber,” *Sci. Rep.* **11**(1), 5173 (2021).
27. H. Apriyanto, O. D. Bernal, M. Cattoen, *et al.*, “Splice Loss Investigation of Single-Mode Fiber and Photonic Crystal Fibers and Its Potential Refractometric Sensing Applications,” *IEEE Sens. Lett.* **8**(8), 1–4 (2024).
28. S. Ando, Y. Watanabe, and T. Matsuura, “Wavelength Dependence of Refractive Indices of Polyimides in Visible and Near-IR Regions,” *Jpn. J. Appl. Phys.* **41**(Part 1, 8), 5254–5258 (2002).
29. A. S. Hicyilmaz and A. C. Bedeloglu, “Applications of polyimide coatings: a review,” *SN Appl. Sci.* **3**(3), 363 (2021).
30. S. Chang, C. C. Hsu, T.-H. Huang, *et al.*, “Heterodyne Interferometric Measurement of the Thermo-Optic Coefficient of Single Mode Fiber,” *Chin. J. Phys.* **38**, 437–442 (2000).
31. C. Shang, B. Fu, J. Tuo, *et al.*, “Soft Biomimetic Fiber-Optic Tactile Sensors Capable of Discriminating Temperature and Pressure,” *ACS Appl. Mater. Interfaces* **15**(46), 53264–53272 (2023).

32. P. I. Gnusin, S. A. Vasil'ev, O. I. Medvedkov, *et al.*, "Reversible changes in the reflectivity of different types of fibre Bragg gratings," *Quantum Electron.* **40**(10), 879–886 (2010).
33. X. Rosello-Mecho, M. Delgado-Pinar, A. Diez, *et al.*, "Measurement of Pockels' coefficients and demonstration of the anisotropy of the elasto-optic effect in optical fibers under axial strain," *Opt. Lett.* **41**(13), 2934–2937 (2016).
34. N. J. Alberto, C. A. Marques, J. L. Pinto, *et al.*, "Three-parameter optical fiber sensor based on a tilted fiber Bragg grating," *Appl. Opt.* **49**(31), 6085–6091 (2010).
35. X. Chen, J. Xu, X. Zhang, *et al.*, "Wide Range Refractive Index Measurement Using a Multi-Angle Tilted Fiber Bragg Grating," *IEEE Photonics Technol. Lett.* **29**(9), 719–722 (2017).
36. E. Chehura, S. W. James, and R. P. Tatam, "Temperature and strain discrimination using a single tilted fibre Bragg grating," *Opt. Commun.* **275**(2), 344–347 (2007).
37. B. Jiang, Z. Bi, S. Wang, *et al.*, "Cascaded tilted fiber Bragg grating for enhanced refractive index sensing," *Chin. Phys. B* **27**(11), 114220 (2018).
38. X. Hu, Y. Liu, H. Wei, *et al.*, "Tilted Bragg grating in a glycerol-infiltrated specialty optical fiber for temperature and strain measurements," *Opt. Lett.* **49**(11), 2869–2872 (2024).
39. L. Martins, B. Kulyk, A. Theodosiou, *et al.*, "Laser-induced graphene from commercial polyimide coated optical fibers for sensor development," *Opt. Laser Technol.* **160**, 109047 (2023).
40. H. C. Gomes, X. Liu, A. Fernandes, *et al.*, "Laser-Induced graphene-based Fabry-Pérot cavity label-free immunosensors for the quantification of cortisol," *Sens. Actuators Rep.* **7**, 100186 (2024).